

# Strain-engineering on the topological type-II Dirac semimetal $\text{NiTe}_2$

P. P. Ferreira,<sup>1,\*</sup> A. L. R. Manesco,<sup>1,2,†</sup> T. T. Dorini,<sup>3</sup> L. E. Correa,<sup>1</sup> G. Weber,<sup>1</sup> A. J. S. Machado,<sup>1</sup> and L. T. F. Eleno<sup>1,‡</sup>

<sup>1</sup>*Computational Materials Science Group (ComputEEL/MatSci),  
Escola de Engenharia de Lorena da Universidade de São Paulo,  
Materials Engineering Department, Lorena – SP, Brazil*

<sup>2</sup>*Kavli Institute of Nanoscience, Delft University of Technology, Delft, The Netherlands*

<sup>3</sup>*Université de Lorraine, CNRS, IJL, Nancy, France*

(Dated: May 25, 2022)

In this preliminary pre-print, the electronic and elastic properties of the type-II Dirac semimetal  $\text{NiTe}_2$ , in equilibrium and under strain, were systematically studied within the scope of density functional theory. The bulk transition metal dichalcogenide  $\text{NiTe}_2$  harbor tilted symmetry-protected Dirac cones derived from p-orbital bands in the Fermi level. The projected band-structure and group analysis show that a single orbital-manifold band-inversion is the mechanism behind the presence of the topologically non-trivial states. In this vein, a plethora of distinct strain profiles are shown to be an effective route to manipulate such electronic features. Small compressive and tensile deformations are enough to control the position and energy level of the Dirac-type excitations in the Brillouin zone, tuning the cone position and relative energy to the Fermi level. It is possible to lower or increase the overlap between the wave functions of low-energy valence-bands states and suppress usual bands, abruptly changing its fermiology — opening the way for electronic phase transitions and a hybrid Dirac semimetal phase. In the next versions, to be released soon, we will provide a minimal effective model for the Dirac cones and derive the mentioned effects of strain using a lattice regularization approach. Additionally, through our investigations of the relationship between electronic and topological phases and its elastic properties, we will propose static-controlling the electronic states by the intercalation of light-metal species into the van der Waals gap, resulting in a similar physical response to the one obtained by dynamical strain-engineering.

## I. INTRODUCTION

With the advent of topology in materials science, uncovering unexplored vistas into physics and the possibility of brand-new electronic devices, our understanding of the nature of quantum matter and its emerging quasiparticle excitations, without counterparts in the standard model of elementary particle physics, has dramatically changed — and is also being continually altered. In the last few years, back to the description of the quantum spin Hall effect in graphene by Kane and Mele<sup>1,2</sup> and the first realization of three-dimensional topological band insulators driven by strong spin-orbit coupling (SOC) effects<sup>3–9</sup>, the proposal of topologically distinct metallic states<sup>10–12</sup>, introducing the Weyl and Dirac semimetals<sup>13</sup>, has drawn a heightened interest. Among their exotic properties, we could highlight the ultrahigh electronic mobility and conductivity<sup>14–17</sup>, negative/giant magnetoresistance<sup>18–20</sup>, chiral anomaly<sup>21–24</sup> and quantum anomalous Hall effect<sup>25–27</sup>, to cite a few examples. Those materials can be viewed as a three-dimensional analogue of graphene, where valence and conduction bands touch at discrete twofold (Weyl) or fourfold (Dirac) degenerate points in the first Brillouin zone and disperse linearly in all momentum directions, forming symmetry-protected massless bulk Weyl/Dirac fermions and exotic surface spin-textures, robust against perturbations<sup>28–32</sup>. In this way, by breaking the inversion or time-reversal symmetries, one Dirac cone will decouple into a pair of opposite-chirality Weyl fermions<sup>33–35</sup>.

Fermions in condensed-matter systems are dictated by crystal space-group symmetry operations — they are not constrained by the Lorentz invariance principle, opposed to the conventional high-energy particles. This brings up to the light a novel bewildering array of Lorentz-violating excitations where the relativistic energy-momentum dispersion explicitly depends on its direction in the momentum space<sup>36</sup>. In condensed-matter systems, one such manifestation is realized by low-energy electronic-states with tilted cone-shaped features in the band-structure, where electron- and hole-pockets touch each other at discrete points in the Fermi surface, giving rise to distinct classes of topological materials: the so-called type-II Weyl and Dirac semimetals<sup>37–42</sup>. The type-II topological semimetals will promote different experimental signatures compared to the type-I candidates, showing, for instance, extremely anisotropic transport and magnetoresistance properties<sup>43–46</sup>.

Within this context, the transition metal dichalcogenide  $\text{NiTe}_2$  was recently rediscovered as a type-II Dirac semimetal<sup>47,48</sup>. Transport measurements reveal a non-saturating linear magnetoresistance and quantum oscillations confirm the existence of a nontrivial Berry phase for the associated light mass carriers<sup>47</sup>. Furthermore, unique topological surface states with chiral spin-texture over a wide range of energies was supported by spin- and angle-resolved photoemission spectroscopy<sup>49</sup>, and possible low-dimensionality- and pressure-induced superconductivity are being considered<sup>48,50,51</sup>. In fact, the intercalation of Ti into van der Waals gap (the space be-

tween two adjacent chalcogenide layers) in NiTe<sub>2</sub> induces a pressure-robust superconducting phase with a critical temperature ( $T_c$ ) close to 4.0 K<sup>48</sup>. It is important to note that NiTe<sub>2</sub> receives much attention due to, among other reasons, the energy position of its massless Dirac fermions, very close to the chemical potential, together with high-quality single-crystals that are relatively easy to obtain<sup>52–54</sup>. Consequently, NiTe<sub>2</sub> becomes a prominent candidate for the next generation of nontrivial devices in spintronics, infrared plasmonics and ultrafast optoelectronics<sup>49</sup>.

In the present work, having discussed the relevance of the subject, we propose, from first-principles electronic-structure calculations, a strain-engineering approach to provide, on NiTe<sub>2</sub>, a controlled way to manipulate its emergent massless quasiparticle low-energy excitations. Our results suggest that, by applying distinct strain modes, we could access different kinds of topological states, such the coexistence of type-I and type-II Dirac fermions in the same band-dispersion, setting the NiTe<sub>2</sub> as an ideal scientific playground to investigate the multiple facets that quantum matter can assume. In parallel, we take the opportunity to provide a systematic description of the electronic-structure of NiTe<sub>2</sub> and its elastic properties.

The manuscript is organized as follows. Sec. II describes in details the computational methods and numerical parameters used in the first-principle electronic-structure calculations. In Sec. III, we present a comprehensive investigation on the electronic and elastic properties of the ground-state structure. Sec. IV shows the key results related to the strain-engineering of the electronic states of NiTe<sub>2</sub> in the vicinity of the Fermi level.

**This manuscript is a preliminary version. Due to the increasing interest on NiTe<sub>2</sub> system, we have decided to release our first-draft results on arXiv. The manuscript will be updated soon with the demonstration that the intercalation of light-metal species, such Li, Na and K, into the van der Waals gap could reproduce the desired physical response as obtained from applying different profiles of stress-strain, acting effectively as a chemical-pressure source inside the crystal-structure. Also, we will provide a minimal effective model within lattice regularization approach to describe the type-II Dirac cones.**

## II. COMPUTATIONAL METHODS

First-principles electronic-structure calculations were carried out in the framework of the Density Functional Theory (DFT) within the Kohn-Sham scheme<sup>55,56</sup>, using the pseudopotential approach as implemented in *Quantum Espresso*<sup>57,58</sup> and some auxiliary post-processing tools<sup>59,60</sup>. The calculations were performed using a series of different approximations for the exchange and correlation (XC) functional, within its relativistic and non-

relativistic form. The considered parametrizations were the local-density-approximation (LDA) of Perdew-Zhang (PZ)<sup>61</sup> and the generalized-gradient-approximation with the Perdew-Burke-Ernzerhof (PBE)<sup>62</sup> parametrization and its modified version, known as PBEsol<sup>63</sup>; as well as non-local functionals, including the van der Waals interactions<sup>64</sup>, namely vdW-DF<sup>65,66</sup>, optB86b-vdW<sup>67</sup> and optB88-vdW<sup>68</sup>. To guarantee the convergence of the energy eigenvalues of the Kohn-Sham self-consistent solution, we have adopted a wave function energy cut-off of 260 Ry (1 Ry  $\approx$  13.6 eV) and a sampling of  $16 \times 16 \times 8$  k-points in the first Brillouin zone according to the Monkhorst-Pack scheme<sup>69</sup>. To compute the electronic properties a denser k-mesh grid was considered, with  $32 \times 32 \times 16$  k-points. All lattice parameters and internal degrees of freedom were fully relaxed in order to reach a ground-state convergence of  $10^{-6}$  Ry in total energy and  $10^{-4}$  Ry/a<sub>0</sub> (a<sub>0</sub>  $\approx$  0.529 Å) for forces acting on the nuclei.

The full second-order elastic stiffness tensor was obtained from a set of deformations imposed on the reference ground-state structures ( $\eta = 0$ ), as implemented in the *ElaStic* tool<sup>70</sup>, taking the second-partial derivative of the total energy with respect to the lagrangian strain:

$$c_{\alpha\beta} = \frac{1}{V_0} \left. \frac{\partial^2 U}{\partial \eta_\alpha \partial \eta_\beta} \right|_{\eta=0}, \quad (1)$$

where  $U$  is the total energy due to the deformation,  $V_0$  is the volume of the undeformed optimised structure and  $\eta_\alpha$  and  $\eta_\beta$  are the lagrangian strains<sup>70</sup>, expressed in Voigt notation, where the Voigt components run from 1 to 6. We have used five different deformation types to obtain the five independent second-order elastic constants of the trigonal symmetry, with a maximum absolute intensity of  $\eta_{max} = 0.05$  for Lagrangian strain, and 15 distorted structures with strain intensities between  $-\eta_{max}$  and  $+\eta_{max}$ , for each deformation type, resulting in a total of 90 deformed structures.

From the stiffness tensor it is also possible to derive macroscopic mechanical moduli and their crystallographic orientation-dependence<sup>71</sup>. Details on this topic are provided in Appendix A.

## III. GROUND-STATE PROPERTIES

NiTe<sub>2</sub> is a layered compound that crystallizes in a trigonal centrosymmetric structure within CdI<sub>2</sub>-prototype (space-group  $P\bar{3}m1$ , number 164). As shown in Fig. 1, a Ni layer is sandwiched between two Te layers, with the stacking of adjacent Te layers mediated by weak van der Waals interactions<sup>72</sup>.

The optimized cell parameters, as well as the relaxed Te-position degree of freedom, satisfying the minimum energy and force condition requirement, are presented in Table I. Regardless of the choice of the exchange and correlation functional for the Kohn-Sham Hamiltonian, the

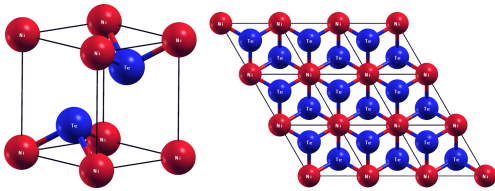


FIG. 1: Trigononal unit cell of  $\text{NiTe}_2$  alongside a top view of a  $3 \times 3 \times 3$  supercell (blue:Te; red: Ni atoms).

TABLE I:  $\text{NiTe}_2$  fully optimized cell-parameters ( $a$  and  $c$ ) and atomic position degree of freedom of Te atoms ( $z_{\text{Te}}$ ) using different XC functionals.

XC functional	$a$ (Å)	$c$ (Å)	$V$ (Å <sup>3</sup> )	$z_{\text{Te}}$
PZ	3.814	5.105	64.31	0.2522
PZ+SOC	3.797	5.186	64.75	0.2511
PBE	3.894	5.372	70.54	0.2442
PBE+SOC	3.897	5.377	70.72	0.2452
vdW-DF	3.971	5.377	73.43	0.2369
optB88-vdW	3.902	5.331	70.29	0.2535
optB86b-vdW	3.863	5.277	68.20	0.2494
Expt. <sup>52</sup>	3.858	5.264	67.85	–
Calc. <sup>73</sup>	3.808	5.236	65.75	–

relative error, compared with the experimental crystallographic data available, for both calculated cell parameters and atomic positions, does not exceed 3% in our calculations. The best results, judging by the structural properties, were obtained with the optB86b-vdW, including non-local corrections. The PBE functional, including spin-orbit coupling effects, which is widely used in the literature, also results in good structural parameters with a small associated error; but, as expected, this type of functional overestimate the distance between adjacent layers, where the van der-Waals interactions play an important role. However, we have observed that spin-orbit coupling effects are more expressive over the electronic energy dispersion than the van der Waals interactions between adjacent layers. Thus, all the results presented in this manuscript, except when explicitly mentioned, correspond to the PBE parametrization including SOC effects.

The six second-order elastic constants  $c_{\alpha\beta}$  necessary to specify the elastic stiffness tensor for a trigonal crystal, calculated with different approximations for the exchange and correlation functional, are listed in Tab. II. The calculated elastic constants show good agreement when compared with the experimental data available (see Table II). In particular, the smallest differences between the theoretical calculation and the experimental data were obtained using the generalized-gradient approximation

and non-local van der Waals corrections. Elastic constants for which van der Waals interactions are relevant, i.e., those that play a role in shear-type strain, such as  $c_{14}$  and  $c_{44}$ , are better predicted by the optB86b-vdW functional, evidencing the weak interaction between the adjacent layers of tellurium. However, when stronger interatomic bonds are required by the deformation, such Ni-Te and Ni-Ni bonds, related to  $c_{11}$ ,  $c_{12}$  and  $c_{33}$ , the GGA-type functionals were able to describe better the medium/strong interactions existing between the electronic states, consequently resulting in a better description of the elastic behavior. It is important to highlight that these findings could be useful for future theoretical attempts on elastic properties of transition-metal dichalcogenides and related compounds. The mechanical

TABLE II: Second order elastic constants (in GPa) calculated for the trigonal structure of  $\text{NiTe}_2$

	$c_{11}$	$c_{12}$	$c_{13}$	$c_{14}$	$c_{33}$	$c_{44}$
PBE	110.8	38.20	22.90	−5.00	45.50	10.20
PBE+SOC	113.7	36.60	27.20	−6.50	45.70	11.20
PZ+SOC	145.5	54.00	43.30	−14.30	76.60	26.80
optB86b-vdW	127.4	47.10	26.80	−9.40	75.70	20.20
Expt. <sup>74</sup>	109.5	41.90	–	−10.70	52.60	20.40
Calc. <sup>73</sup>	147.6	50.80	44.10	7.91	83.90	17.58

stability can be easily verified through the Mouhat and Coudert criteria<sup>75</sup>, that, for trigonal crystals, assume the following conditions:

$$\begin{aligned}
 c_{11} &> |c_{12}|, \quad c_{44} > 0, \\
 c_{13}^2 &< \frac{1}{2}c_{33}(c_{11} + c_{12}), \\
 c_{14}^2 &< \frac{1}{2}c_{44}(c_{11} - c_{12}) = c_{44}c_{66}.
 \end{aligned} \tag{2}$$

All the conditions are completely fulfilled using the elastic constants presented in Tab. II. Therefore, the  $\text{NiTe}_2$ , in its bulk configuration, is, indeed, mechanically stable. Additionally, the elastic anisotropy and mechanical modulus were also computed from the stiffness tensor. The main results are presented in details in Appendix A.

The projected density of states (DOS) of  $\text{NiTe}_2$  is presented in Fig. 2(a). The populated Fermi level, as can be seen, confirms the semimetal nature of the compound. The total DOS at the Fermi energy ( $E_F$ ) is 1.67 states/eV, with nearly 59% of the electronic states derived from Te-5p orbitals and 34% from Ni-3d manifold.

In Fig. 2(b) is shown the projected electronic band-structure, within the vicinity of the Fermi level, along the high-symmetry points in the first Brillouin zone of the trigonal  $\text{NiTe}_2$  structure. The contribution of the dominating 5p orbitals from Te, in the band diagram,

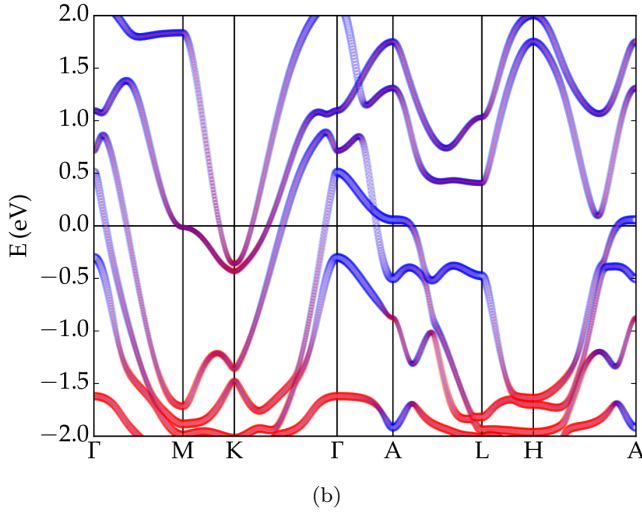
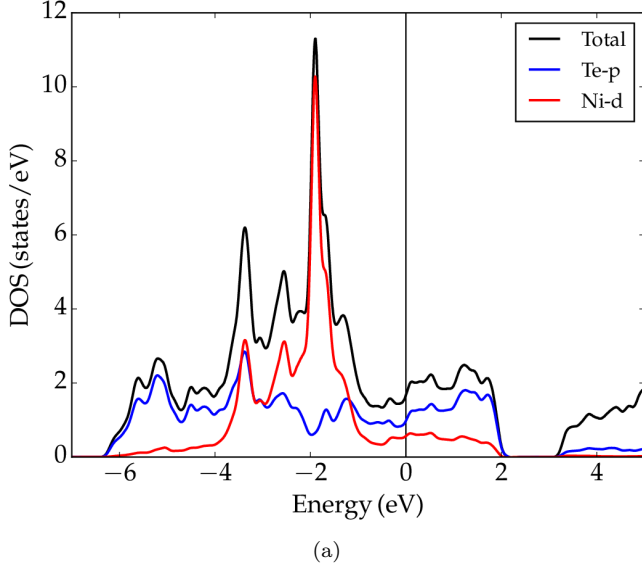


FIG. 2:  $\text{NiTe}_2$  projected density of states (a) and electronic band-structure (b) with SOC. The colors indicate, respectively, the orbital contribution of the Te-5p (blue) and Ni-3d (red) orbitals in the wavefunctions of the electronic states.

are indicated by the blue dots, while the contribution of the 3d orbitals from Ni are represented by the red dots. There are four distinct bands crossing the Fermi level, giving rise to the four independent sheets of the Fermi surface, as shown in Fig. 3. Despite  $\text{NiTe}_2$  being an almost quasi-2 dimensional material due to its layered structure, weakly coupled along the  $c$  direction, the Fermi surface possesses a strong 3-dimensional character. The sheets consist of (a) a closed hole-pocket, around the  $\Gamma$ -point (the center of the Brillouin zone), surrounded by (b) an opened hole-pocket with a very complex fermiology that develops along the  $\Gamma$ -A direction ( $k_z$  direction), where A is the center of the face of a hexagon. In addition, electron-pockets compose the

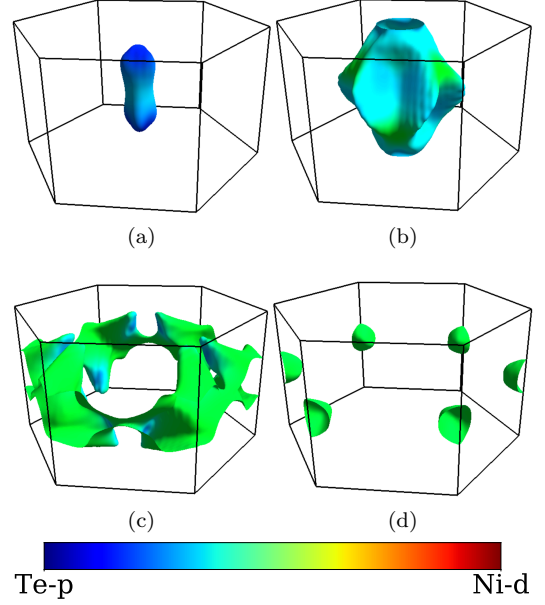


FIG. 3: (a)-(d) The four independent sheets of the Fermi surface of the  $\text{NiTe}_2$  compound. The color map shows the contribution of Te-5p (blue) and Ni-3d (red) manifold to the electronic wave function. The green regions indicate a strong hybridization.

surface (c) around the K-point (middle of an edge joining two rectangular faces) and (d) M-point (center of a rectangular face). The explicit contribution of the Ni-d and Te-p orbitals can be seen through the color scale in Figure 3. The hole-pockets are mainly composed by the electronic states derived from Te-p orbitals, whereas the electron-pockets are derived, partially, from Ni-d states, with a strong hybridization with Te-p states.

The most important feature in the energy dispersion of the  $\text{NiTe}_2$  is found along the  $\Gamma$ -A direction, as detailed in Fig. 4. The valence band and the conduction band touch each other at a discrete point along  $\Gamma$ -A. As  $\text{NiTe}_2$  has the presence of both inversion- and time-reversal-symmetry, each band is doubly degenerate. Therefore, the linear crossing of the valence and conduction band originates a pair of gapless Dirac nodes (fourfold degenerate) located at  $\mathbf{k}_D = (0, 0, \pm 0.665)$ , in units of  $\pi/c$  in the first Brillouin zone. The bulk tilted Dirac cone lies very close to the Fermi energy, at  $E_D = 0.15 \text{ eV}$ . For comparison, the Pd- and Pt-based dichalcogenides host Dirac points deep below the Fermi level, between 0.6 and 1.2 eV<sup>40–42</sup>.

The trigonal crystal-field with the strong intralayer hybridization between the Te-p manifold of different sites breaks the original threefold degeneracy of the  $p$ -orbitals, resulting in bonding and anti-bonding combinations of the in-plane ( $p_x, p_y$ ) and out-of-plane states ( $p_z$ ). The spin-orbit coupling further splits the  $p$ -derived electronic states due to the double group symmetry representation, including the spin degree of freedom. As the  $\Gamma$ -A direc-

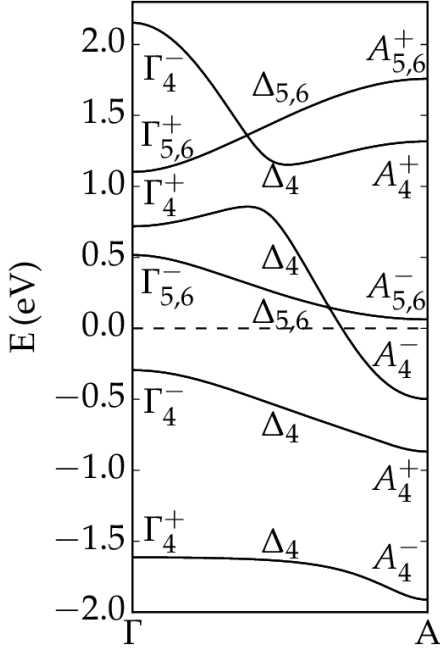


FIG. 4: Detailed electronic band-structure with the irreducible representations and parity analysis along the  $\Gamma$ -A direction.

tion holds the  $C_3$  rotational symmetry (the system is invariant under rotations by  $2\pi/3$  around the  $z$  axes), the  $p$ -derived states will split into two distinct irreducible representations,  $R_4$  (derived from out-of-plane  $p_z$  orbitals) and  $R_{5,6}$  (derived from in-plane  $p_{x,y}$ -orbitals), being  $R_4$  bidimensional and  $R_{5,6}$  degenerate. The irreducible representations and its parities in high-symmetry points are shown in Fig. 4.

Considering that the out-of-plane  $p_z$ -derived states will have a larger hopping along the out-of-plane direction ( $k_z$ ) than the in-plane  $p_{x,y}$ -derived states, a series of band crossings are expected to occur along this direction. The crossing between the  $R_4^\pm$  and  $R_{5,6}^\mp$  states will lead to the bulk type-II Dirac node, harboring pseudo-relativistic Lorentz-violating quasiparticles. This crossing is symmetrically allowed, since we have distinct irreducible representations available, and is protected against hybridization/gap-opening mechanisms due to  $C_3$  rotational symmetry. On the other hand, the crossings between  $R_4^\pm$  and  $R_4^\mp$  distinct bands are not allowed, and noticing that they have opposite parities, their hybridization leads to a gap with band inversion (the parity inversion is easily seen at  $A_4^+$  and  $A_4^-$  states just below the Fermi level). Therefore, a  $\mathbb{Z}_2$  order is established, as presented in topological insulators. However, the bulk Dirac cone formation in  $\text{NiTe}_2$  is very distinct to topological insulators since, in this case, only a single-orbital manifold is required. Thus, it is expected the presence of topological surface states residing inside the gap. This single-orbital manifold mechanism of bulk Dirac cones is

widely discussed elsewhere<sup>76,77</sup>.

In addition, just above the Dirac cone located in the close vicinity of the Fermi level, there is another band crossing giving rise to type-I Dirac fermions at  $\mathbf{k}_D = (0, 0, \pm 0.388)$  with  $R_4^\pm$  and  $R_{5,6}^\mp$  representations and energy level  $E_D = 1.36$  eV: just a few meV bigger than the low-energy excitations found in the Pd- and Pt-based dichalcogenides.

#### IV. STRAIN-ENGINEERING

In this section, we will investigate how different strain-stress states modify the electronic properties of  $\text{NiTe}_2$ . To do so, calculations were performed with three types of strain: uniaxial deformation along the  $[001]$  direction ( $z$ -axis); biaxial deformation within the basal plane, perpendicular to the  $z$ -direction; and isostatic deformation. For each type, at least 6 deformations were performed, going from -5% to +5% with respect to the fully relaxed lattice parameters.

##### A. Effects of strain in the band-structure

Fig. 5 shows selected strained band-structures with the same wave function projections used in Fig. 2, taking into account spin-orbit coupling effects. In a first analysis, it is possible to conclude that finite lagrangian strains, with small spatial perturbations, are capable to accurately control the following electronic features: hybridization of the atomic orbital states; dispersion of the bands (transport properties), as a consequence of the hybridization; the chemical potential and the fermiology.

By bringing the multiple layers that build up  $\text{NiTe}_2$  or the atoms inside those layers close together, we increase the hybridization of electronic wave functions. In this way, the associated quasi-particles become increasingly delocalized, culminating, then, in bands with high effective velocity along the Brillouin zone, as can be seen in the deformations  $\eta = (-0.05, -0.05, -0.05)$ ,  $\eta = (-0.05, -0.05, 0)$  and  $\eta = (0, 0, -0.05)$ ; that is, cases (a), (c), and (e) in Figure 5. This stronger hybridization can also be seen in the band projection onto the Te- $p$  and Ni- $d$  orbitals, where a stronger overlap between these two orbitals is visible. Otherwise, as we move the atoms away from their first neighbors, decreasing the interatomic interaction, we give rise to more localized wave functions, resulting in bands with lower effective velocities, that can be seen in the deformed structures in cases (b), (d), and (f); that is,  $\eta = (0.05, 0.05, 0.05)$ ,  $\eta = (0.05, 0.05, 0)$  and  $\eta = (0, 0, 0.05)$ .

By manipulating the effective velocities, it is possible to tune the tilt parameter of the Dirac cones in the close vicinity of the Fermi level, promoting, in this manner, significant controlled changes in the anisotropic transport properties of the relativistic Dirac-type excitations present in the system. Also, the cone position with



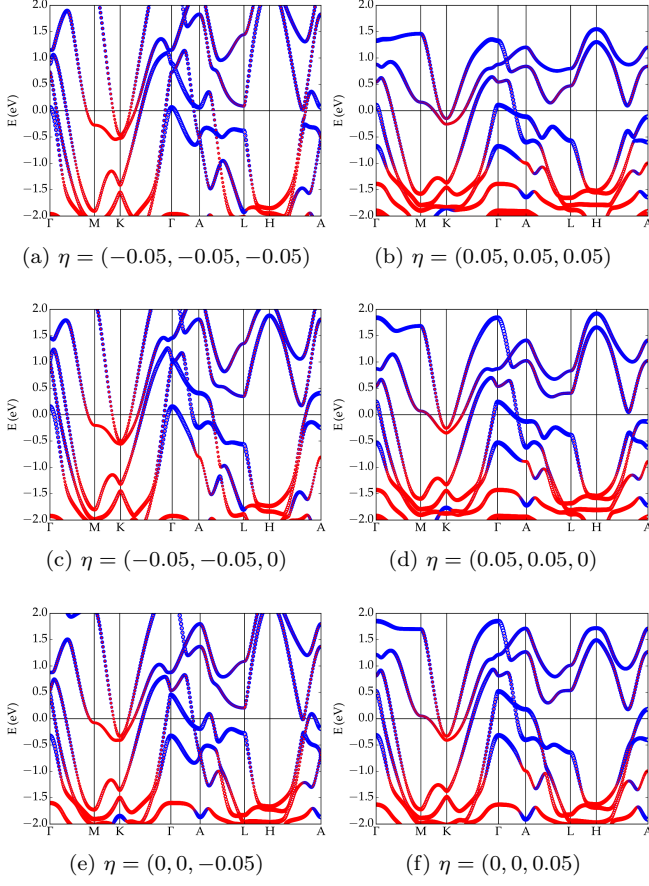


FIG. 5: (a)-(f) Projected band-structure of  $\text{NiTe}_2$  for some selected deformed structures. Red points indicate the Ni-d orbital contribution and blue points the Te-p derived states.

respect to the Fermi level is profoundly modified, causing, as a possible effect, an effective change in the chirality and spin-texture of the topological edge states — originated from the band inversion mechanism of the  $R_4$ -derived states — as long as the Dirac node moves across the Fermi energy. Hence, by means of band-structure analysis, strain could provide continuous and reversible tuning of the spin-momentum locked surface states of the  $\text{NiTe}_2$ , making this compound a promising metallic candidate for spin-based applications.

We can also check that trivial bands crossing the Fermi level are suppressed when the structure is expanded, and some extra bands become part of the Fermi surface when the structure is compressed, possibly attenuating the topological manifestations. To illustrate this phenomenon, the Fermi surface onto the velocity operator under isostatic deformation is shown in Figure 6 for deformations (a)  $\eta = (-0.05, -0.05, -0.05)$  and (b)  $\eta = (0.05, 0.05, 0.05)$ . When the structure is compressed an additional branch shows up in the Fermi surface along the  $\Gamma$ -A direction. The extra branch corresponds to the band with irreducible representation  $R_4$  derived from the

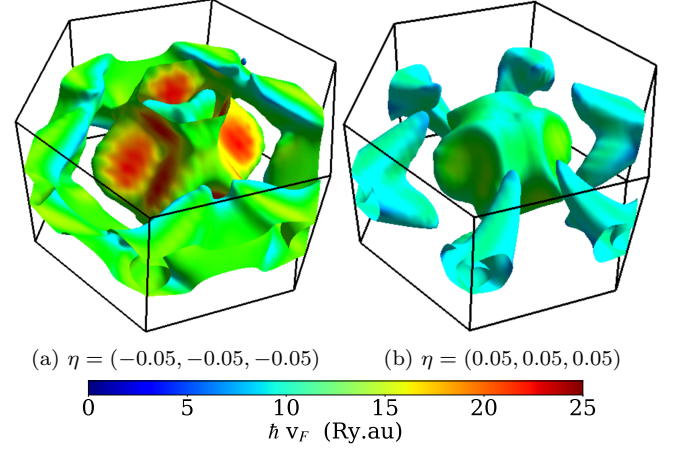


FIG. 6: Fermi surfaces of  $\text{NiTe}_2$  under isostatic strain. The color map indicates the magnitude of the Fermi velocity.

in-plane  $p_{x,y}$  orbitals. This band, before with a low-dispersion along the out-of-plane direction, due to its symmetry, deforms in response to the increasing overlap between the different wave functions (Ni-d and Te-p orbitals), acquiring delocalized states and increasing, therefore, the energy of its electronic states in relation to the chemical potential of the structure at 0 K, resulting in the crossing of those states with the zero energy level.

On the other hand, despite the persistence of four distinct branches of the Fermi surface for the tensile structure, its composition changes dramatically when compared to the deformation-free structure. Distancing the adjacent layers, we suppress the crossing along the direction  $A$ - $L$  and create an intersection in the direction  $\Gamma$ - $A$ . As a result, we will have a disconnected hole-pocket and an electron-pocket surrounding the  $\Gamma$ -point and two electron-pockets surrounding the  $K$ -point, with a much lower Fermi velocity when compared with the situation without deformation or under the effect of an isostatic pressure, reflecting the low effective velocities. It is possible to see that the Dirac point will appear in the contact between the electron-pocket and the hole-pocket that are located around  $\Gamma$  as we bring the chemical potential to  $E = E_D$ . If we lower the chemical potential further, the fermionic packages will disconnect again and the electron-pockets will gradually decrease in size.

From this perspective, we can conclude that isoenergetic surfaces evolve rapidly and undergo a sudden change in their topology due to the deformation of the network, paving the way for Lifshitz transitions<sup>78,79</sup>.

## B. Dynamically controlling the Dirac cone

Figure 7 shows the evolution of the energy level and position in the Brillouin zone, in units of  $\pi/c$ , of the Type-II Dirac node as a function of: (i) biaxial deformation

within the  $x$ - $y$  plane  $(\eta, \eta, 0)$ ; (ii) uniaxial strain along the  $z$ -axis,  $(0, 0, \eta)$ ; and (iii) isostatic pressure,  $(\eta, \eta, \eta)$ .

For a biaxial strain, the Dirac cone moves towards the Fermi level and to the  $A$  high-symmetry point, at the border of the Brillouin zone, crossing the chemical potential in approximately  $\eta = 2\%$ ; for a state of compression, the cone departs from the Fermi level, reaching around  $0.6\text{ eV}$  at  $-5\%$ , and approaches the center of the BZ. The opposite effect is observed for the deformation  $(0, 0, \eta)$ . In this situation, the cone will cross  $E_F$  around  $-2\%$ , coming close to  $0.4\text{ eV}$  at  $+5\%$ . Therefore, for an isostatic deformation, the type-II Dirac point dynamics could be described as a combination of uniaxial and biaxial deformations. The crossing at the Fermi level occurs only close to  $+4\%$ , and the curve, as shown, suggests that a compression greater than  $6\%$  may bring the cone below  $0\text{ eV}$ , bringing it closer to the border of the Brillouin zone. It is also worth noticing that, extrapolating both the Dirac node energy as well as the position of trivial bands (check Fig. 5), one might get a situation with only non-trivial bands at the Dirac node energy, just a few hundreds of meV below the Fermi level.

In addition to the direct control of the position and energy level of the Dirac cones through small deformations in the crystal structure, it is possible, by the same process, access new topological states, as shown in Fig. 8, which summarizes the energy evolution of the irreducible representations of the bands that harbor the type-II Dirac cone in the vicinity of the Fermi level. The state  $\Gamma_4^+$  has an even dependency with isostatic pressure, decreasing its energy in relation to  $E_F$  for isostatic deformations

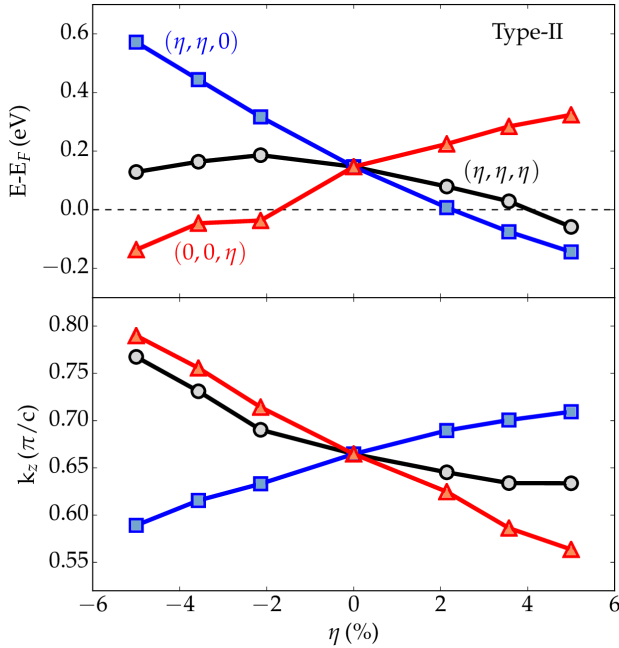


FIG. 7: Evolution of the energy and position in the Brillouin zone for the type-II Dirac point in function of different deformations.

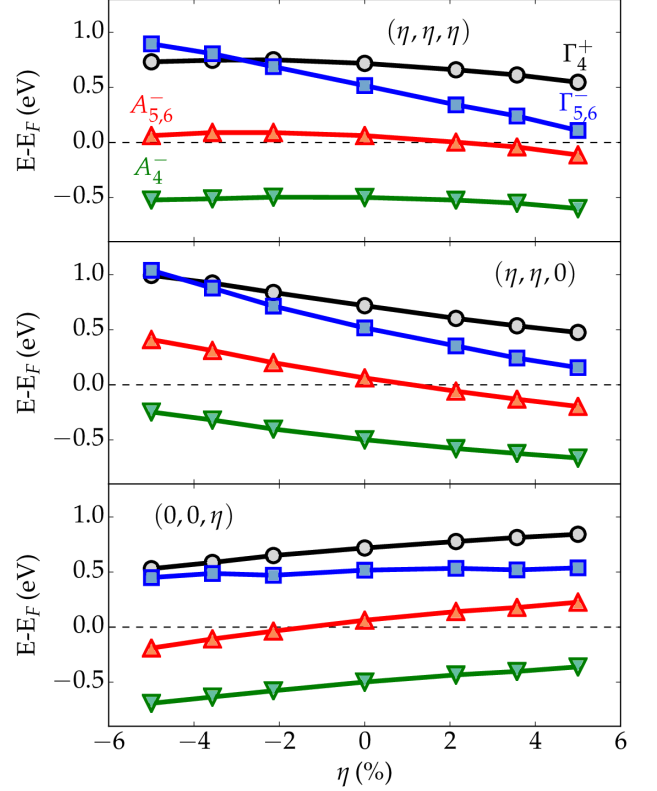


FIG. 8: Energy evolution of the irreducible representations  $\Gamma_4^+$ ,  $\Gamma_{5,6}^-$ ,  $A_{5,6}^-$  e  $A_4^-$  for the deformations  $(\eta, \eta, \eta)$ ,  $(\eta, \eta, 0)$  e  $(0, 0, \eta)$ .

greater than  $-2\%$ . The symmetry state  $\Gamma_{5,6}^-$ , on the other hand, has an odd dependency. Combined, both behaviors result in a crossing between the bands with different irreducible representations. Thus, a new pair of untilted (type-I) Dirac cones will be created close to the point  $\Gamma$ , for approximately  $\eta = -3\%$  and  $E - E_F = 0.8\text{ eV}$ . This same effect is found for uniaxial and biaxial deformations. In the case of  $(\eta, \eta, 0)$ , the type-I Dirac pair will form at  $\eta \approx -4.2\%$ , and for  $(0, 0, \eta)$  the crossing between the bands will occur close to  $\eta = 6\%$ . Thus, by manipulating the system,  $\text{NiTe}_2$  is able to harbor three-dimensional interacting Dirac fermions in the same energy band with very distinct energy-momentum dispersion.

The coexistence of type-I and type-II Dirac cones provides a route to unique and unexplored magnetoresistive and transport signatures. While Dirac type-I semimetals exhibit a negative magnetoresistance in all directions<sup>15,17</sup>, the transport properties in Dirac type-II semimetals are expected to be extremely anisotropic and present a negative magnetoresistance only in directions where the potential term is higher than the kinetic term<sup>36</sup>.  $\text{PdTe}_2$ <sup>80</sup> and the family of compounds  $\text{CaAgBi}$ <sup>81</sup> are one of the few materials in which the coexistence of Dirac cones of type-I and type-II is expected to happen in the same band energy. However,  $\text{NiTe}_2$  arouse a particular interest due to the position of the cones in relation

to the Fermi level, comprising very low-energy states, and also because of the small distance between them in the Brillouin zone, representing, therefore, an ideal platform for the study of the interaction between different surface states and quasi-particles with different pseudo-relativistic signatures.

The next question one might ask is: How would be the experimental signatures and the practical effects resulting from the manipulation of the Dirac points using deformation? For that, we will start thinking, for simplicity's sake, about the classical measurements of resistivity and magnetization. Magnetoresistance for conventional metals grows quadratically in low fields and tends to a saturation value in high fields. However, in materials where conventional charge carriers and Dirac fermions coexist and populate the Fermi surface, the magnetoresistance curve as a function of the applied magnetic field reveals an additional (and predominant) linear term to the quadratic term<sup>82,83</sup>. Thus, it is expected that, with the presence of Dirac cones at the Fermi level, the contributions of these quasi-particles to the magnetoresistance will be accentuated, thus increasing the contribution from the linear term of the NiTe<sub>2</sub> response to intense magnetic fields. Also, in many topological semimetals it is possible to observe a pronounced growth of the resistivity curve in the low temperature regime increasing the field. Enhancing the contribution from pseudo-relativistic carriers, combined with suppression of carriers

derived from the other non-relativistic metallic bands, it is expected that this signature will be evidenced, resulting, invariably, in a significant increase in the magnetoresistance.

In summary, our calculations point that we can precisely control the massless low-energy electronic excitations, harbored in the volume and surface, providing a building block for applications in electronics, spintronics and ultra-fast optoelectronics. It is important to highlight that the strain-engineering to manipulate correlated electronic systems can be done in real electronic devices using piezoelectric actuators, even in mechanically delicate samples<sup>84</sup>.

## ACKNOWLEDGMENTS

We gratefully acknowledge the financial support of the Fundação de Amparo à Pesquisa do Estado de São Paulo (FAPESP) under Procs. 18/10835-6, 16/10167-8, 18/08819-2, 19/14359-7 and 19/05005-7. This study was also financed in part by the Coordenação de Aperfeiçoamento de Pessoal de Nível Superior (CAPES) - Brasil - Finance Code 001. The research was carried out using high-performance computing resources made available by the Superintendência de Tecnologia da Informação (STI), Universidade de São Paulo.

- 
- \* Corresponding author: pedroferreira@usp.br  
† Corresponding author: antoniolrm@usp.br  
‡ Corresponding author: luizeleno@usp.br
- <sup>1</sup> C. L. Kane and E. J. Mele, Physical review letters **95**, 146802 (2005).
  - <sup>2</sup> C. L. Kane and E. J. Mele, Physical review letters **95**, 226801 (2005).
  - <sup>3</sup> L. Fu, C. L. Kane, and E. J. Mele, Physical review letters **98**, 106803 (2007).
  - <sup>4</sup> L. Fu and C. L. Kane, Physical Review B **76**, 045302 (2007).
  - <sup>5</sup> D. Hsieh, D. Qian, L. Wray, Y. Xia, Y. S. Hor, R. J. Cava, and M. Z. Hasan, Nature **452**, 970 (2008).
  - <sup>6</sup> D. Hsieh, Y. Xia, L. Wray, D. Qian, A. Pal, J. Dil, J. Osterwalder, F. Meier, G. Bihlmayer, C. Kane, *et al.*, Science **323**, 919 (2009).
  - <sup>7</sup> Y. Xia, D. Qian, D. Hsieh, L. Wray, A. Pal, H. Lin, A. Bansil, D. Grauer, Y. S. Hor, R. J. Cava, *et al.*, Nature physics **5**, 398 (2009).
  - <sup>8</sup> H. Zhang, C.-X. Liu, X.-L. Qi, X. Dai, Z. Fang, and S.-C. Zhang, Nature physics **5**, 438 (2009).
  - <sup>9</sup> Y. Chen, J. G. Analytis, J.-H. Chu, Z. Liu, S.-K. Mo, X.-L. Qi, H. Zhang, D. Lu, X. Dai, Z. Fang, *et al.*, science **325**, 178 (2009).
  - <sup>10</sup> O. Vafek and A. Vishwanath, Annu. Rev. Condens. Matter Phys. **5**, 83 (2014).
  - <sup>11</sup> A. Burkov, Nature materials **15**, 1145 (2016).
  - <sup>12</sup> H. Weng, X. Dai, and Z. Fang, Journal of Physics: Condensed Matter **28**, 303001 (2016).
  - <sup>13</sup> N. Armitage, E. Mele, and A. Vishwanath, Reviews of Modern Physics **90**, 015001 (2018).
  - <sup>14</sup> C. Shekhar, A. K. Nayak, Y. Sun, M. Schmidt, M. Nicklas, I. Leermakers, U. Zeitler, Y. Skourski, J. Wosnitza, Z. Liu, *et al.*, Nature Physics **11**, 645 (2015).
  - <sup>15</sup> T. Liang, Q. Gibson, M. N. Ali, M. Liu, R. J. Cava, and N. P. Ong, Nature materials **14**, 280 (2015).
  - <sup>16</sup> Y. Zhao, H. Liu, C. Zhang, H. Wang, J. Wang, Z. Lin, Y. Xing, H. Lu, J. Liu, Y. Wang, *et al.*, Physical Review X **5**, 031037 (2015).
  - <sup>17</sup> J. Xiong, S. K. Kushwaha, T. Liang, J. W. Krizan, M. Hirschberger, W. Wang, R. J. Cava, and N. P. Ong, Science **350**, 413 (2015).
  - <sup>18</sup> X. Huang, L. Zhao, Y. Long, P. Wang, D. Chen, Z. Yang, H. Liang, M. Xue, H. Weng, Z. Fang, *et al.*, Physical Review X **5**, 031023 (2015).
  - <sup>19</sup> H. Li, H. He, H.-Z. Lu, H. Zhang, H. Liu, R. Ma, Z. Fan, S.-Q. Shen, and J. Wang, Nature communications **7**, 10301 (2016).
  - <sup>20</sup> W. Gao, N. Hao, F.-W. Zheng, W. Ning, M. Wu, X. Zhu, G. Zheng, J. Zhang, J. Lu, H. Zhang, *et al.*, Physical review letters **118**, 256601 (2017).
  - <sup>21</sup> A. Zyuzin and A. Burkov, Physical Review B **86**, 115133 (2012).
  - <sup>22</sup> S. Parameswaran, T. Grover, D. Abanin, D. Pesin, and A. Vishwanath, Physical Review X **4**, 031035 (2014).
  - <sup>23</sup> C.-L. Zhang, S.-Y. Xu, I. Belopolski, Z. Yuan, Z. Lin, B. Tong, G. Bian, N. Alidoust, C.-C. Lee, S.-M. Huang, *et al.*, Nature communications **7**, 10735 (2016).



- <sup>24</sup> A. A. Burkov and Y. B. Kim, Physical review letters **117**, 136602 (2016).
- <sup>25</sup> F. Haldane, Physical review letters **93**, 206602 (2004).
- <sup>26</sup> G. Xu, H. Weng, Z. Wang, X. Dai, and Z. Fang, Physical review letters **107**, 186806 (2011).
- <sup>27</sup> H. Weng, R. Yu, X. Hu, X. Dai, and Z. Fang, Advances in Physics **64**, 227 (2015).
- <sup>28</sup> X. Wan, A. M. Turner, A. Vishwanath, and S. Y. Savrasov, Physical Review B **83**, 205101 (2011).
- <sup>29</sup> Z. Liu, B. Zhou, Y. Zhang, Z. Wang, H. Weng, D. Prabhakaran, S.-K. Mo, Z. Shen, Z. Fang, X. Dai, *et al.*, Science **343**, 864 (2014).
- <sup>30</sup> H. Yi, Z. Wang, C. Chen, Y. Shi, Y. Feng, A. Liang, Z. Xie, S. He, J. He, Y. Peng, *et al.*, Scientific reports **4**, 6106 (2014).
- <sup>31</sup> S.-M. Huang, S.-Y. Xu, I. Belopolski, C.-C. Lee, G. Chang, B. Wang, N. Alidoust, G. Bian, M. Neupane, C. Zhang, *et al.*, Nature communications **6**, 7373 (2015).
- <sup>32</sup> S.-Y. Xu, I. Belopolski, N. Alidoust, M. Neupane, G. Bian, C. Zhang, R. Sankar, G. Chang, Z. Yuan, C.-C. Lee, *et al.*, Science **349**, 613 (2015).
- <sup>33</sup> Z. Wang, Y. Sun, X.-Q. Chen, C. Franchini, G. Xu, H. Weng, X. Dai, and Z. Fang, Physical Review B **85**, 195320 (2012).
- <sup>34</sup> A. Zyuzin, S. Wu, and A. Burkov, Physical Review B **85**, 165110 (2012).
- <sup>35</sup> R. Okugawa and S. Murakami, Physical Review B **89**, 235315 (2014).
- <sup>36</sup> A. A. Soluyanov, D. Gresch, Z. Wang, Q. Wu, M. Troyer, X. Dai, and B. A. Bernevig, Nature **527**, 495 (2015).
- <sup>37</sup> K. Deng, G. Wan, P. Deng, K. Zhang, S. Ding, E. Wang, M. Yan, H. Huang, H. Zhang, Z. Xu, *et al.*, Nature Physics **12**, 1105 (2016).
- <sup>38</sup> K. Koepnick, D. Kasinathan, D. Efremov, S. Khim, S. Borisenko, B. Büchner, and J. van den Brink, Physical Review B **93**, 201101 (2016).
- <sup>39</sup> G. Chang, S.-Y. Xu, D. S. Sanchez, S.-M. Huang, C.-C. Lee, T.-R. Chang, G. Bian, H. Zheng, I. Belopolski, N. Alidoust, *et al.*, Science Advances **2**, e1600295 (2016).
- <sup>40</sup> K. Zhang, M. Yan, H. Zhang, H. Huang, M. Arita, Z. Sun, W. Duan, Y. Wu, and S. Zhou, Physical Review B **96**, 125102 (2017).
- <sup>41</sup> H.-J. Noh, J. Jeong, E.-J. Cho, K. Kim, B. Min, and B.-G. Park, Physical review letters **119**, 016401 (2017).
- <sup>42</sup> M. Yan, H. Huang, K. Zhang, E. Wang, W. Yao, K. Deng, G. Wan, H. Zhang, M. Arita, H. Yang, *et al.*, Nature communications **8**, 257 (2017).
- <sup>43</sup> Y. Wang, E. Liu, H. Liu, Y. Pan, L. Zhang, J. Zeng, Y. Fu, M. Wang, K. Xu, Z. Huang, *et al.*, Nature communications **7**, 13142 (2016).
- <sup>44</sup> F. Chen, H. Lv, X. Luo, W. Lu, Q. Pei, G. Lin, Y. Han, X. Zhu, W. Song, and Y. Sun, Physical Review B **94**, 235154 (2016).
- <sup>45</sup> N. Kumar, Y. Sun, N. Xu, K. Manna, M. Yao, V. Süß, I. Leermakers, O. Young, T. Förster, M. Schmidt, *et al.*, Nature communications **8**, 1642 (2017).
- <sup>46</sup> J. Lai, Y. Liu, J. Ma, X. Zhuo, Y. Peng, W. Lu, Z. Liu, J. Chen, and D. Sun, ACS nano **12**, 4055 (2018).
- <sup>47</sup> C. Xu, B. Li, W. Jiao, W. Zhou, B. Qian, R. Sankar, N. D. Zhigadlo, Y. Qi, D. Qian, F.-C. Chou, *et al.*, Chemistry of materials **30**, 4823 (2018).
- <sup>48</sup> B. de Lima, R. de Cassia, F. Santos, L. Correa, T. Grant, A. Manesco, G. Martins, L. Eleno, M. Torikachvili, and A. Machado, Solid State Communications **283**, 27 (2018).
- <sup>49</sup> B. Ghosh, D. Mondal, C.-N. Kuo, C. S. Lue, J. Nayak, J. Fujii, I. Vobornik, A. Politano, and A. Agarwal, Physical Review B **100**, 195134 (2019).
- <sup>50</sup> F. Zheng, X.-B. Li, P. Tan, Y. Lin, L. Xiong, X. Chen, and J. Feng, Physical Review B **101**, 100505 (2020).
- <sup>51</sup> T. Li, K. Wang, C. Xu, Q. Hou, H. Wu, J.-Y. Ge, S. Cao, J. Zhang, W. Ren, X. Xu, *et al.*, arXiv preprint arXiv:1911.07173 (2019).
- <sup>52</sup> J. F. H. L. Monteiro, M. B. Marciniak, A. R. Jurelo, E. C. Siqueira, F. T. Dias, and J. L. P. Júnior, Journal of Crystal Growth **478**, 129 (2017).
- <sup>53</sup> B. Zhao, W. Dang, Y. Liu, B. Li, J. Li, J. Luo, Z. Zhang, R. Wu, H. Ma, G. Sun, *et al.*, Journal of the American Chemical Society **140**, 14217 (2018).
- <sup>54</sup> Q. Liu, F. Fei, B. Chen, X. Bo, B. Wei, S. Zhang, M. Zhang, F. Xie, M. Naveed, X. Wan, *et al.*, Physical Review B **99**, 155119 (2019).
- <sup>55</sup> P. Hohenberg and W. Kohn, Physical review **136**, B864 (1964).
- <sup>56</sup> W. Kohn and L. J. Sham, Physical review **140**, A1133 (1965).
- <sup>57</sup> P. Giannozzi, S. Baroni, N. Bonini, M. Calandra, R. Car, C. Cavazzoni, D. Ceresoli, G. L. Chiarotti, M. Cococcioni, I. Dabo, *et al.*, Journal of physics: Condensed matter **21**, 395502 (2009).
- <sup>58</sup> P. Giannozzi, O. Andreussi, T. Brumme, O. Bunau, M. B. Nardelli, M. Calandra, R. Car, C. Cavazzoni, D. Ceresoli, M. Cococcioni, *et al.*, Journal of Physics: Condensed Matter **29**, 465901 (2017).
- <sup>59</sup> A. Kokalj, Journal of Molecular Graphics and Modelling **17**, 176 (1999).
- <sup>60</sup> M. Kawamura, Computer Physics Communications **239**, 197 (2019).
- <sup>61</sup> J. P. Perdew and A. Zunger, Physical Review B **23**, 5048 (1981).
- <sup>62</sup> J. P. Perdew, K. Burke, and M. Ernzerhof, Physical review letters **77**, 3865 (1996).
- <sup>63</sup> J. P. Perdew, A. Ruzsinszky, G. I. Csonka, O. A. Vydrov, G. E. Scuseria, L. A. Constantin, X. Zhou, and K. Burke, Physical review letters **100**, 136406 (2008).
- <sup>64</sup> F. Tran, L. Kalantari, B. Traoré, X. Rocquefelte, and P. Blaha, Physical Review Materials **3**, 063602 (2019).
- <sup>65</sup> M. Dion, H. Rydberg, E. Schröder, D. C. Langreth, and B. I. Lundqvist, Physical review letters **92**, 246401 (2004).
- <sup>66</sup> M. Dion, H. Rydberg, E. Schröder, D. Langreth, and B. I. Lundqvist, Physical Review Letters **95**, 109902 (2005).
- <sup>67</sup> J. Klimeš, D. R. Bowler, and A. Michaelides, Journal of Physics: Condensed Matter **22**, 022201 (2009).
- <sup>68</sup> J. Klimeš, D. R. Bowler, and A. Michaelides, Physical Review B **83**, 195131 (2011).
- <sup>69</sup> H. J. Monkhorst and J. D. Pack, Physical review B **13**, 5188 (1976).
- <sup>70</sup> R. Golezorkhtabar, P. Pavone, J. Spitaler, P. Puschnig, and C. Draxl, Computer Physics Communications **184**, 1861 (2013).
- <sup>71</sup> P. Ferreira, T. Dorini, F. Santos, A. Machado, and L. Eleno, Materialia **4**, 529 (2018).
- <sup>72</sup> S. Manzeli, D. Ovchinnikov, D. Pasquier, O. V. Yazyev, and A. Kis, Nature Reviews Materials **2**, 17033 (2017).
- <sup>73</sup> J.-Q. Lei, K. Liu, S. Huang, X.-C. Mao, B.-S. Hou, J. Tan, and X.-L. Zhou, Chemical Physics Letters **687**, 250 (2017).
- <sup>74</sup> M. Sato and K. Abe, Journal of Physics C: Solid State Physics **12**, L613 (1979).

- <sup>75</sup> F. Mouhat and F.-X. Coudert, Physical review B **90**, 224104 (2014).
- <sup>76</sup> M. Bahramy, O. Clark, B.-J. Yang, J. Feng, L. Bawden, J. Riley, I. Marković, F. Mazzola, V. Sunko, D. Biswas, *et al.*, Nature materials **17**, 21 (2018).
- <sup>77</sup> O. Clark, F. Mazzola, I. Marković, J. Riley, J. Feng, B. Yang, K. Sumida, T. Okuda, J. Fujii, I. Vobornik, *et al.*, Electronic Structure **1**, 014002 (2019).
- <sup>78</sup> F. Liu, J. Li, K. Zhang, S. Peng, H. Huang, M. Yan, N. Li, Q. Zhang, S. Guo, X. Lü, *et al.*, SCIENCE CHINA Physics, Mechanics & Astronomy **62**, 48211 (2019).
- <sup>79</sup> M. Qi, C. An, Y. Zhou, H. Wu, B. Zhang, C. Chen, Y. Yuan, S. Wang, Y. Zhou, X. Chen, *et al.*, Physical Review B **101**, 115124 (2020).
- <sup>80</sup> R. Xiao, P. Gong, Q. Wu, W. Lu, M. Wei, J. Li, H. Lv, X. Luo, P. Tong, X. Zhu, *et al.*, Physical Review B **96**, 075101 (2017).
- <sup>81</sup> C. Chen, S.-S. Wang, L. Liu, Z.-M. Yu, X.-L. Sheng, Z. Chen, and S. A. Yang, Physical Review Materials **1**, 044201 (2017).
- <sup>82</sup> A. Abrikosov, Physical Review B **58**, 2788 (1998).
- <sup>83</sup> A. Abrikosov, Journal of Physics A: Mathematical and General **36**, 9119 (2003).
- <sup>84</sup> J. Park, J. M. Bartlett, H. M. Noad, A. Stern, M. E. Barber, M. König, S. Hosoi, T. Shibauchi, A. P. Mackenzie, A. Steppke, *et al.*, arXiv preprint arXiv:2003.11444 (2020).
- <sup>85</sup> R. Hill, Proceedings of the Physical Society. Section A **65**, 349 (1952).
- <sup>86</sup> S. Pugh, The London, Edinburgh, and Dublin Philosophical Magazine and Journal of Science **45**, 823 (1954).
- <sup>87</sup> X.-Q. Chen, H. Niu, D. Li, and Y. Li, Intermetallics **19**, 1275 (2011).

## Appendix A: Elastic anisotropy and mechanical properties

The second-order elastic constants  $c_{\alpha\beta}$  also provide valuable information about the mechanical response of a compound, given a certain applied strain condition. The  $c_{11}$  and  $c_{33}$  constants, for instance, represent the resistance to an uniaxial deformation along the [100] and [001] directions, respectively, while the  $c_{44}$  elastic constant is related to the resistance to a shear deformation in the  $(hk0)$  planes. Therefore, the NiTe<sub>2</sub> compound, basically constituted by a set of layers that are periodically repeated along the  $c$ -direction, with weak interactions acting between these fundamental blocks, has a low resistance to shearing in planes parallel to the tellurium sheets, with  $c_{44} = 20.2$  GPa, according to the optB86-vdW functional. In the [100] and [001] crystallographic directions, we find Ni-Te and Ni-Ni bonds, offering, therefore, greater resistance to structural changes along these directions. Thus, the constant  $c_{11} = 110.8$  GPa reflects a strong intralayer interaction, whereas the value of 45.5 GPa for the  $c_{33}$  elastic constant indicates that when strain is applied in the [001] direction, the region between tellurium layers will undergo a significant structural change, since in the van der Waals gap there is a small resistance to deformation. But, on the other hand, the nickel and tellurium will continue to inter-

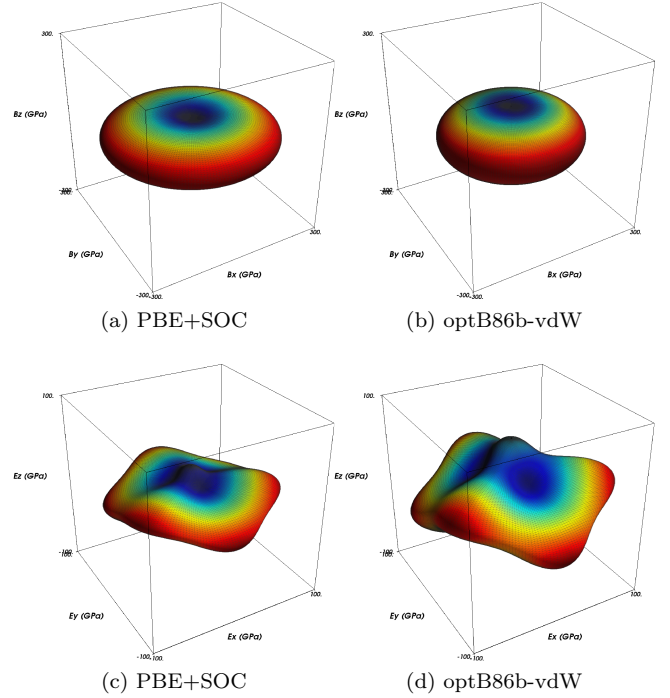


FIG. 9: Directional dependence of the reciprocal linear compressibility  $B_c$  (a-b) and Young's modulus  $E$  (c-d) for NiTe<sub>2</sub> (in GPa) using different exchange and correlation functionals.

act in order to establish ionic/covalent bonds, preserving the mechanical stability and exerting some resistance. The mechanical properties within the Voigt-Reuss-Hill approximation<sup>85</sup> are shown in Tab. III. It is interesting to note the B/G ratio for the different exchange and correlation functionals. The B/G ratio is widely used as a general measure of ductility<sup>86</sup>. Values higher than 1.75 indicate a ductile regime, while an B/G ratio less than 1.75 indicate that the compound has a brittle behavior. The calculated value for the B/G ratio, therefore, shows that NiTe<sub>2</sub>, surprisingly, presents a good ductibility for an intermetallic compound. This assessment is consistent with a Poisson ratio higher than 0.26<sup>87</sup>. However, the PBE+SOC approach, as expected, overestimate the ductile regime when compared to the optB86b-vdW values. This result establishes that NiTe<sub>2</sub> is, therefore, a decent candidate for strain-engineering.

Knowledge of the degree of anisotropy in the single crystal elastic properties is essential to strain-engineering applications. The calculated reciprocal linear compressibility ( $B_c$ ) and Young's modulus ( $E$ ) directional dependencies for several exchange and correlation functionals are shown in Fig. 9. The reciprocal linear compressibility has small anisotropy, presenting a flattened spherical shape as function of the crystallographic orientation. On the other hand, the Young's modulus has a strong elastic anisotropy. It's possible to visualize a large resistance to elastic deformation in the [110] direction and a

TABLE III: Bulk modulus (B), shear modulus (G), Young modulus (E) and Poisson's ratio ( $\nu$ ) for NiTe<sub>2</sub> according to the Voigt-Heuss-Hill approximation. All values are in the unit of GPa (except dimensionless quantities).

	$B_V$	$B_R$	$B_H$	$G_V$	$G_R$	$G_H$	$B/G$	$E_V$	$E_R$	$E_H$	$\nu_V$	$\nu_R$	$\nu_H$
PBE	48.34	38.60	43.47	23.54	15.60	19.57	2.22	60.75	41.24	51.04	0.29	0.32	0.30
PBE+SOC	50.58	40.56	45.57	24.34	16.05	20.19	2.26	62.93	42.53	52.79	0.29	0.33	0.31
PZ+SOC	72.09	64.26	68.17	34.98	27.80	31.39	2.17	90.34	72.90	81.65	0.29	0.31	0.30
optB86b-vdW	59.12	53.84	56.48	31.44	25.41	28.43	1.99	80.11	65.88	73.03	0.27	0.30	0.28
Calc. <sup>73</sup>	-	-	70.12	-	-	28.75	2.44	-	-	50.95	-	-	0.32

slight resistance in the [001] direction. Such mechanical manifestation occurs due to, as discussed based on the second-order elastic constants, the weak van der Waals interactions between adjacent Te-layers and a stronger in-plane electronic density. It is also important to depict the changes in the elastic anisotropy profiles for different exchange and correlation functionals. Fig. 10 shows a planar projection of the Young's modulus using PBE+SOC and optB86b-vdW for directions in (110) crystallographic planes. The different mechanical resistance between the [001] and [110] directions is clear. The Young's modulus projection curve within (110) plane is visibly tilted. The origin of this elastic behavior is the opposite positions of the Te atoms in the unit cell, generating this anisotropy. Since different exchange and correlation functionals provide different force and energy minimizations to the Te atomic position degree of freedom, as well as different interatomic interactions and effective electronic densities, the net effect is a rotation of the Young's modulus projection, changing its tilting angle and its absolute value.

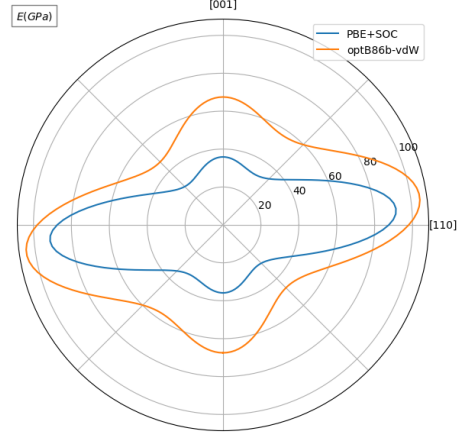


FIG. 10: Polar plot of the Young's modulus  $E$  (in GPa) in the (110) crystallographic plane.